


## Long-distance coupling of standing spin waves mediated by a charge current

Qian Chen,<sup>1,2</sup> Zhaocong Huang ,<sup>1</sup> Bin Fang,<sup>2</sup> Rongxin Li,<sup>2</sup> Yang Xiao,<sup>3</sup> Hengguo Lai,<sup>2</sup> Qingjie Guo,<sup>1</sup> Weiming Lv,<sup>2</sup> Lei Wang,<sup>1</sup> Shuai Dong,<sup>1</sup> Ya Zhai,<sup>1,\*</sup> Zhongming Zeng,<sup>2,4,†</sup> and Ke Xia<sup>1,‡</sup>

<sup>1</sup>Key Laboratory of Quantum Materials and Devices of Ministry of Education, School of Physics, Southeast University, Nanjing 211189, China

<sup>2</sup>Nanofabrication Facility, Suzhou Institute of Nano-Tech and Nano-Bionics, Chinese Academy of Sciences, Suzhou, Jiangsu 215123, China

<sup>3</sup>College of Science, Nanjing University of Aeronautics and Astronautics, Nanjing 210016, China

<sup>4</sup>Nanchang Key Laboratory of Advanced Packaging and the Division of Nano-Devices and Technologies, Jiangxi Institute of Nanotechnology, Nanchang 330200, China



(Received 4 April 2023; revised 18 July 2024; accepted 8 November 2024; published 18 December 2024)

We propose an experimentally feasible dynamic coupling of ferromagnets mediated by a charge current in a nonmagnetic heavy metal. Dynamic magnetic moments generate a spin current via spin pumping, subsequently converted into charge current through the inverse spin Hall effect. This charge current, in turn, generates another spin current via the spin Hall effect, exerting an anti-damping-like torque on the adjacent ferromagnet. Our theoretical framework reveals the dissipative nature of this dynamic coupling, characterized by energy-level attraction that promotes synchronization of frequency, phase, and amplitude information. Experimental validation is realized on submicrometer-sized Py rectangles interconnected by Pt strips using spin-torque ferromagnetic resonance techniques. The standing spin waves excited in Py arrays exhibit high spin pumping efficiency, enabling the demonstration of the proposed dynamic coupling. A notably long coupling length exceeding 2  $\mu\text{m}$  is achieved. These findings underscore a promising pathway for integrated magnonic devices, particularly in applications related to spin synchronization and transmission.

DOI: [10.1103/PhysRevB.110.224427](https://doi.org/10.1103/PhysRevB.110.224427)

Effective interaction and synchronization among magnonic devices are crucial for advancing spintronics research [1,2]. Previous studies have extensively investigated various coupling mechanisms such as magnetic exchange interactions [3,4], dipolar interactions [4,5], and spin transfer effects [6–8]. Most of these interactions are significantly constrained by characteristic length scales. For nanoscale devices, dipolar coupling typically attenuates over hundreds of nanometers, whereas exchange interactions and spin transfer effects remain effective only within distances of a few nanometers.

To overcome these inherent limitations, recent studies have proposed various methodologies. A notable approach involves photon-mediated magnon coupling [9–12], typically utilizing microwave cavity modes, where the strength of coupling depends on cavity quality, spin density, and magnetic damping. This necessitates stringent criteria for material selection and device architecture in magnonic applications. Additionally, there are indications that magnon coupling can also be facilitated by phonons [13,14], yet the high sensitivity of phonon frequencies to material structure imposes inevitable constraints on the design and integration of magnonic devices. Recent theoretical investigations have introduced an innovative strategy involving dynamic coupling mediated by electric currents in nonmagnetic metals, offering promising avenues

for future research and development in this field [15]. This approach capitalizes on the spin Hall magnetoresistance (SMR) effect, which induces an additional spin torque that capable of synchronizing the ferromagnets. This kind of dynamic coupling is not constrained by interferromagnet distances as it relies on the propagation of charge currents. Despite its promising theoretical foundations, experimental validation of this dynamic coupling mechanism remains elusive. The modest additional spin torque induced by the SMR effect poses challenges for experimental detection, primarily due to the involvement of triple charge-spin interconversion processes, resulting in its magnitude being two orders of magnitude smaller than conventional spin torque.

In this study, we propose an experimentally viable approach for charge-mediated coupling of ferromagnets through spin pumping and spin Hall effects. Based on this framework, a spin current originating from spin precession within the ferromagnet converts into a charge current through inverse spin Hall effect (ISHE) [16–19]. This charge current subsequently traverses a non-magnetic strip to reach an adjacent ferromagnet, converting into an other spin current via the spin Hall effect (SHE) [20], exerting an anti-damping-like torque on the magnetization of the neighboring ferromagnet [21–24]. In contrast to the SMR-based model, this strategy involves two consecutive charge-spin interconversion processes, thereby rendering the resultant torques more amenable to experimental detection. Our work verifies the existence of this dynamic coupling effect both theoretically and experimentally, expanding the scope for the design of coupled magnonic devices beyond conventional limits.

\*Contact author: yazhai@seu.edu.cn

†Contact author: zmeng2012@sinano.ac.cn

‡Contact author: kexia@seu.edu.cn

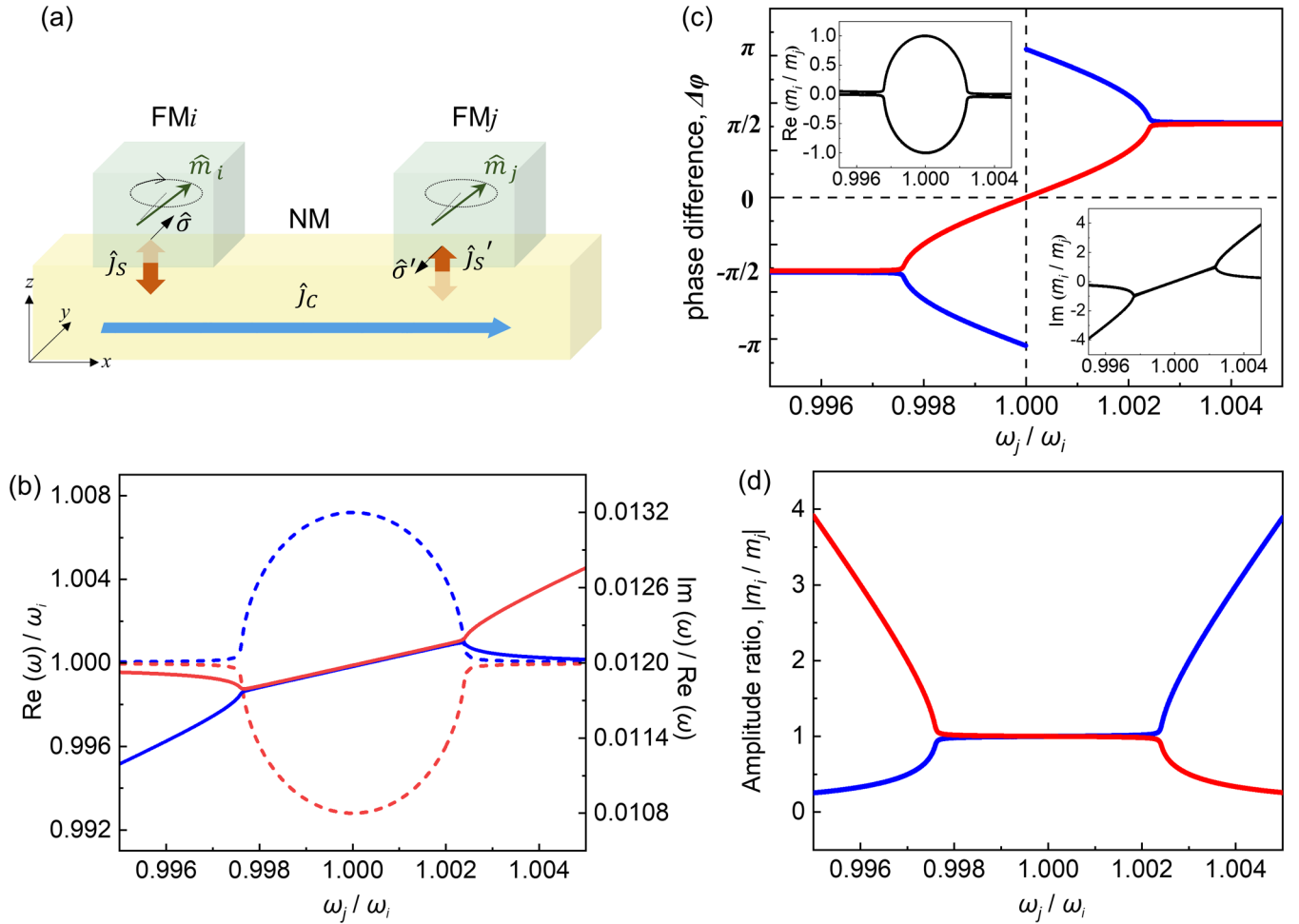


FIG. 1. (a) Schematic structure of the system for dynamic coupling. (b) The real part  $\text{Re}(\omega)$  (solid lines, left axis) and the normalized imaginary part  $\text{Im}(\omega)/\text{Re}(\omega)$  (dashed lines, right axis) of the natural frequencies for various ratios  $\omega_j/\omega_i$ . (c) The phase difference  $\Delta\phi$  between  $\hat{m}_i$  and  $\hat{m}_j$  as a function of the ratio of the intrinsic frequencies of FMs. The insets show the real and imaginary parts of  $\hat{m}_i/\hat{m}_j$ . (d) The amplitude ratio of  $\hat{m}_i$  and  $\hat{m}_j$  for various ratios  $\omega_j/\omega_i$ .

The system depicted in Fig. 1(a) comprises two ferromagnets, FM<sub>*l*</sub> (where  $l = i, j$ ), situated on a nonmagnetic substrate NM within a closed electrical circuit. When subjected to external excitation, the magnetizations of these ferromagnets undergo precession. Due to the spin pumping effect, a spin current  $\hat{J}_S$  generated by the precessing magnetization within FM<sub>*i*</sub> can be expressed as

$$J_S \hat{\sigma} = \frac{\hbar}{4\pi} G_r \left( \vec{m}_i \times \frac{d\vec{m}_i}{dt} \right),$$

where  $G_r$  is the real part of the spin mixing conductance at FM/NM interface [7,25–27]. The induced spin current  $\hat{J}_S$  flows in  $-\hat{z}$  direction, from FM to NM, with the spin polarization of  $\hat{\sigma}$ .  $\hat{J}_S$  undergoes conversion into a charge current  $\hat{J}_C$  via ISHE,

$$\hat{J}_C = \frac{e\theta_{SH} G_r}{2\pi} \left( \vec{m}_i \times \frac{d\vec{m}_i}{dt} \right) \times \hat{z},$$

where  $\theta_{SH}$  is the spin Hall angle. Then  $\hat{J}_C$  transfers to the adjacent ferromagnet (FM<sub>*j*</sub>) through the NM strip, converting

into another spin current  $\hat{J}_S'$  with a polarization  $\hat{\sigma}'$  and flows in  $\hat{z}$  direction as

$$J_S \hat{\sigma} = -\theta_{SH}^2 \frac{\hbar G_r}{4\pi} \left( \vec{m}_i \times \frac{d\vec{m}_i}{dt} \right).$$

The spin current  $\hat{J}_S'$  then exerts an anti-damping-like spin torque  $\tau_{DL}$  on FM<sub>*j*</sub>:

$$\tau_{DL} = -\frac{\gamma \hbar \theta_{SH}^2 G_r}{4\pi \mu_0 M_{SF}} \left( \vec{m}_i \times \frac{d\vec{m}_i}{dt} \right),$$

where  $M_s$  and  $t_F$  are the saturation magnetization and thickness of the ferromagnetic layer. During this process, magnetizations in FMs can interact with each other through the charge current in the NM. The magnetization dynamics in FM<sub>*l*</sub> can be described by the modified Landau-Lifshitz-Gilbert equation:

$$\begin{aligned} \frac{d\hat{m}_l}{dt} = & -\gamma \hat{m}_l \times H_{\text{eff},l} + \alpha_l \left( \hat{m}_l \times \frac{d\hat{m}_l}{dt} \right) + \hat{\alpha}'_l \left( \hat{m}_l \times \frac{d\hat{m}_l}{dt} \right) \\ & - \hat{\alpha}''_l \left( \hat{m}_l \times \frac{d\hat{m}_l}{dt} \right), \end{aligned}$$

where  $\bar{l} = j, i$  for  $l = i, j$ .  $\gamma$  is the gyromagnetic ratio.  $\alpha_l$  and  $\hat{\alpha}'_l$  represent the Gilbert damping constant of FMI and the damping enhancement due to spin pumping effect. The intrinsic frequencies of two FMs  $\omega_i$  and  $\omega_j$  are decided by the corresponding effective fields within the magnetic systems, which equal to  $\gamma H_{\text{eff},i}$  and  $\gamma H_{\text{eff},j}$  respectively. In the experimental process, variations in system architecture and material properties may lead to discrepancies. Therefore, we introduce an adjustment factor  $A$  and define  $\hat{\alpha}''_l = A \times \frac{\gamma \hbar \theta_{SH}^2 G_r}{4\pi \mu_0 M_{SF}}$ . The linearized equations of motion in the absence of driving force are solved by the form  $\propto e^{-i\omega t}$  with two complex-valued natural frequencies  $\omega$  and definite circular polarization. Based on previous experimental reports, we have selected parameters  $\alpha_l = 0.0068$ ,  $\hat{\alpha}'_l = 0.0052$ ,  $G_r = 2.6 \times 10^{19} \text{ m}^{-2}$  and  $\theta_{SH} = 0.1$ , respectively [26,28]. Here we use  $\hat{\alpha}''_l = 0.0012$ , and a quantitative discussion of dynamic coupling with respect to  $\hat{\alpha}''_l$  is provided in Supplemental Material section S1 [29].

The solid lines in Fig. 1(b) show the real part of  $\omega$  for various ratios  $\omega_j/\omega_i$ . It is observed that near  $\omega_j/\omega_i = 1$  (with  $|\omega_j/\omega_i - 1| < 2\alpha''_l$ ), the precession of magnetic moments exhibits coupling, and the resonance frequencies  $\omega_i$  and  $\omega_j$  are locked around  $(\omega_j + \omega_i)/2$ . In contrast to the coupling dominated by magnetic exchange interaction that induces level repulsion between hybridized modes, the dynamic coupling here is governed by the dampinglike term, thereby possessing the dissipative nature which exhibits level attraction [11,26,30–34]. This non-Hermitian property highlights compelling potential for topological information processing. In addition, from the variation of the imaginary part of  $\omega$  with respect to  $\omega_j/\omega_i$  shown by dashed lines in Fig. 1(b), it is found that dissipation decreases in the symmetric (acoustic) mode and increases in the antisymmetric (optic) mode within the coupling region. During ferromagnetic resonance experiments, acoustic modes with lower damping yield stronger signals, thereby exhibiting dynamic coupling in the system as linewidth reduction, as elaborated in Supplemental Material section S1 [29].

To explore its potential for synchronizer applications, we analyze the phase and amplitude characteristics of two magnetization precessions. The phase difference between  $\vec{m}_i$  and  $\vec{m}_j$  can be obtained through the argument of  $\vec{m}_i \vec{m}_j$  in the complex plane, as shown in Fig. 1(c). It is observed that dynamic coupling enables synchronous precession, both in-phase and anti-phase, when the intrinsic frequencies of the two ferromagnets are closely matched. Moreover, we find that the amplitudes of  $\vec{m}_i$  and  $\vec{m}_j$  are tightly synchronized to a nearly uniform value across the entire coupling region, as illustrated in Fig. 1(d). These observations highlight the retention of spin information during transport processes.

Based on the theoretical framework outlined above, experimental investigations are conducted to substantiate this dynamic coupling. We use Permalloy (Py), a common ferromagnetic material, as the FM layer, and Pt as the NM layer. Motivated by pioneering research in spin dynamic detection of submicrometer-sized Py rectangles using stripline ferromagnetic resonance and anisotropic magnetoresistance (AMR) spin rectification [35], we designed our experiment with Py (10 nm) rectangular arrays deposited on Pt (8 nm) microstrips. Employing the spin torque ferromagnetic reso-

nance (ST-FMR) technique enabled us to achieve significant magnetodynamic signals crucial for identifying evidence of dynamic coupling. Note that the current source in the circuit is used to assist with measuring the device resistance and transmitting the DC current, as discussed in detail in Supplemental Material Section S2 [29]. Schematic structure of the experimental system and the scanning electron microscopy (SEM) image of the device are presented in Fig. 2(a). The main structure of the device consists of Py rectangles with the width of  $w$ , the length of  $l$ , and an edge-to-edge distance of  $\Delta$ . The samples are fabricated into devices connecting to coplanar waveguides via multistep lithography processes and integrated with the ST-FMR setup [28]. Details on the structure and fabrication procedures of the device are presented in the Supplemental Material section S3 [29]. To excite spin precessions, an rf current  $I_{\text{rf}}$  is applied along the Pt strip, and an external magnetic field  $H$  is applied in the film plane at a  $45^\circ$  angle with respect to the  $I_{\text{rf}}$ . At this magnetic field angle, both the rectified voltage and the ISHE signal are maximized [36], which facilitates the collection of more information related to spin dynamics. All measurements are conducted at room temperature.

Figure 2(b) depicts the typical FMR spectrum observed from a sample with dimensions  $w = 1 \mu\text{m}$ ,  $l = 1.5 \mu\text{m}$ , and  $\Delta = 300 \text{ nm}$ . Two distinct resonance peaks are clearly discernible. According to micromagnetic simulations [37,38], these two modes correspond to confined modes in Py elements, the quasiuniform precession mode M0 and the standing spin-wave (SSW) mode M1. Their corresponding spatial distributions of magnetic moment precession intensities are illustrated in Fig. 2(c). Both modes are confined to the central region of the Py element due to edge demagnetization effects. Detailed simulation analyses are provided in the Supplemental Material section S4 [29]. The detected FMR spectra can be accurately fitted with a sum of symmetrical and antisymmetrical Lorentzian functions, with the fitting process details provided in the Supplemental Material section S5 [29]. This fitting yields information including the symmetric ( $V_S$ ) and antisymmetric ( $V_A$ ) components, resonance fields ( $H_r$ ), and linewidths ( $\Delta H$ ) of the two modes. The frequency dependence of the extracted  $H_r$  for M0 and M1 are shown in Fig. 2(d). To quantitatively understand the mode structure, a dipole-exchange dispersion of spin wave is used [39–41]:

$$f = \frac{\gamma \mu_0}{2\pi} \left\{ \left[ H + \frac{2A}{\mu_0 M_s} k^2 + M_s \left( 1 - \frac{kt_F}{2} \right) \right] \times \left[ H + \frac{2A}{\mu_0 M_s} k^2 + M_s \frac{kd}{2} \sin^2(\varphi) \right] \right\}^{\frac{1}{2}},$$

where  $\gamma$ ,  $A$ ,  $M_s$  and  $t_F$  denote, respectively, the gyromagnetic ratio, the exchange stiffness, the saturation magnetization, and the thickness of Py.  $H$  is the applied external magnetic field, and  $\varphi$  is the angle between the wave vector  $k$  and  $H$ . In a Py rectangle, spin waves in  $x$  and  $y$  directions are superimposed with each other so that  $k = \frac{(p-\Delta p)\pi}{l} \hat{x} + \frac{(q-\Delta q)\pi}{w} \hat{y}$ , where  $p$  and  $q$  are the mode numbers.  $\Delta p$  and  $\Delta q$  represent the pinning coefficients, which are defined to be positive. By fitting experimental results with the dispersion equation, we confirm that the mode numbers ( $p, q$ ) for M0 and M1 are (1, 1) and

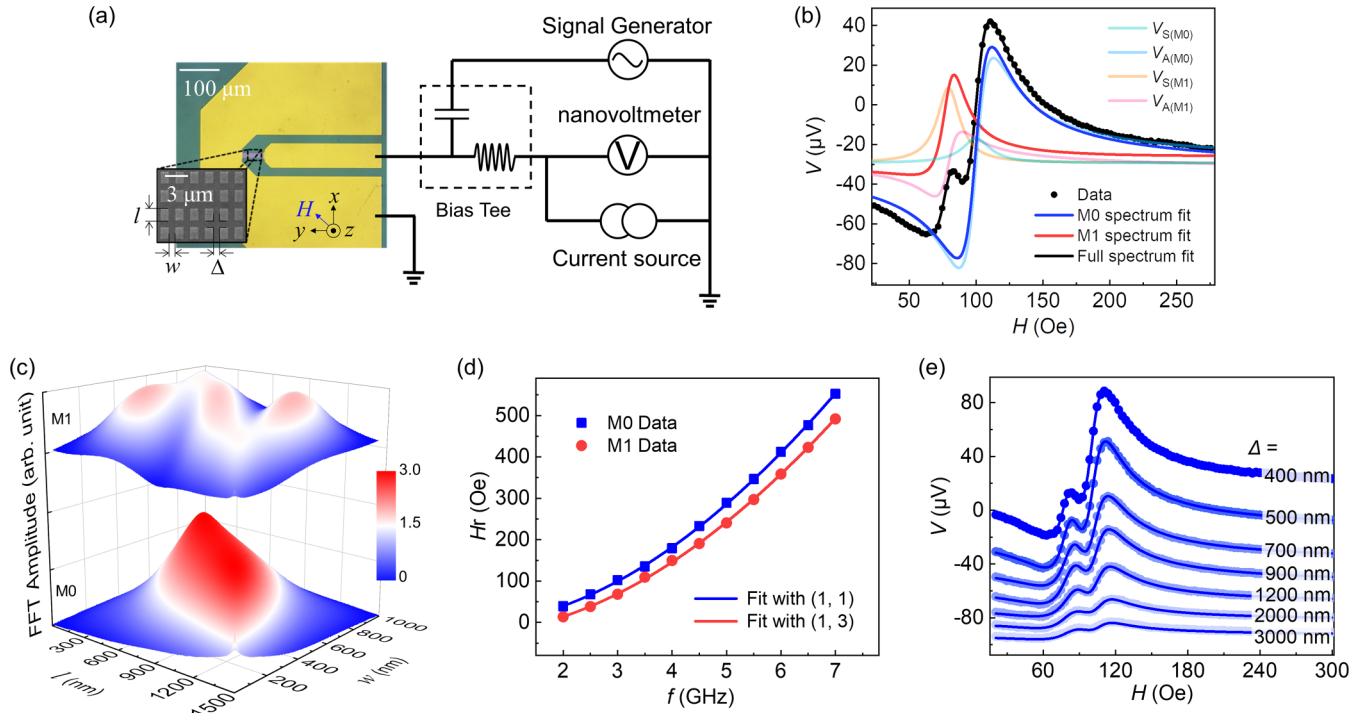


FIG. 2. (a) Schematic structure of the experimental system. The inset is the SEM image of the device. (b) Typical FMR spectrum detected from the sample with  $w = 1 \mu\text{m}$ ,  $l = 1.5 \mu\text{m}$  and  $\Delta = 300 \text{ nm}$  at 3 GHz. Solid lines are fitting results using Eq. (1). (c) Spatial fast Fourier transformation (FFT) of the spin precession obtained by simulation. (d) Frequency dependence of the resonance field for M0 and M1. (e) FMR spectra detected from samples with different array distances. The microwave power is kept at 15 dBm during ST-FMR measurements.

(1, 3) respectively, which agrees well with the simulation result presented in Fig. 2(c).

To investigate the correlations between these precession modes and the spin current, the line shape and intensity of the detected voltage are analyzed. In ST-FMR measurements, the collected symmetric voltage signal  $V_S$  is typically proportional to the spin current generated within the system. The spin current arises from two sources: spin current converted from the rf electric current via SHE, and spin current generated from spin pumping [42,43]. The former source involves the rf spin-orbit torque (SOT), which induces a modification in the AMR of the system, resulting in rectified voltage. In the latter case, spin current derived from spin pumping is converted into a charge current through the ISHE [44]. Therefore, the symmetric component  $V_S$  of the voltage comprises the ISHE voltage and the rectified voltage of the AMR induced by SOT. On the other hand, apart from the SOT, the Oersted field in the system also affects the precession of the magnetization, thus contributing to the alternating AMR. This effect, caused by the rf Oersted field, typically leads to an antisymmetric output  $V_A$  of the dc voltage [28,43]. Figure 3(a) illustrates the ratio of  $V_S$  to  $V_A$  for M0 and M1 measured on samples with varied Py rectangle sizes and  $\Delta = 300 \text{ nm}$ . It is observed that  $V_S/V_A$  for M1 is approximately five times greater than that for M0. This discrepancy implies a significantly larger spin current in the standing spin wave mode compared to the quasiuniform precession mode. In previous studies, enhanced spin pumping efficiency for spin waves has been observed in YIG/Pt heterostructures [45,46]. However, the underlying

physical mechanism remains unclear. The heightened spin current in the SSW mode is further elucidated by the power dependency of voltage intensity ( $V = V_S + V_A$ ) as illustrated in Fig. 3(b). While the voltage intensity of M0 exhibits a linear correlation with the microwave power  $P_{\text{rf}}$ , the voltage intensity of M1 displays a nonlinear response, which can be parsed into square root and linear relationships. This behavior may be associated with the larger spin accumulation in the Pt layer induced by M1, resulting in the spin backflow, which causes the square root dependence of the output voltage on the excitation power [18,45,47]. In Supplemental Material section S6 [29], we examine the discrepancies in these modes affecting spin pumping, positing that the large spin current

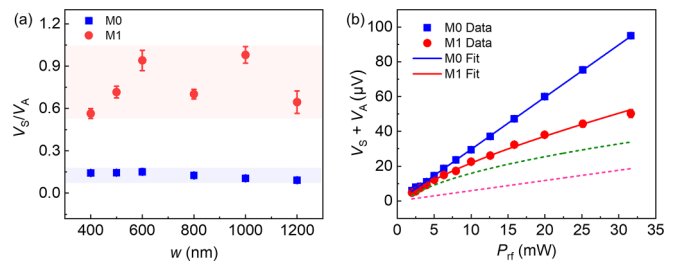


FIG. 3. (a) Ratios of the symmetry and antisymmetry components of the output voltage for samples with different Py rectangle sizes and  $\Delta = 300 \text{ nm}$ . The frequency of the rf current is 3 GHz. (b) Power dependence of M0 and M1. The dashed green and magenta lines represent, respectively, the square root and linear components of the  $P_{\text{rf}}$  dependence of M1 voltage intensity.

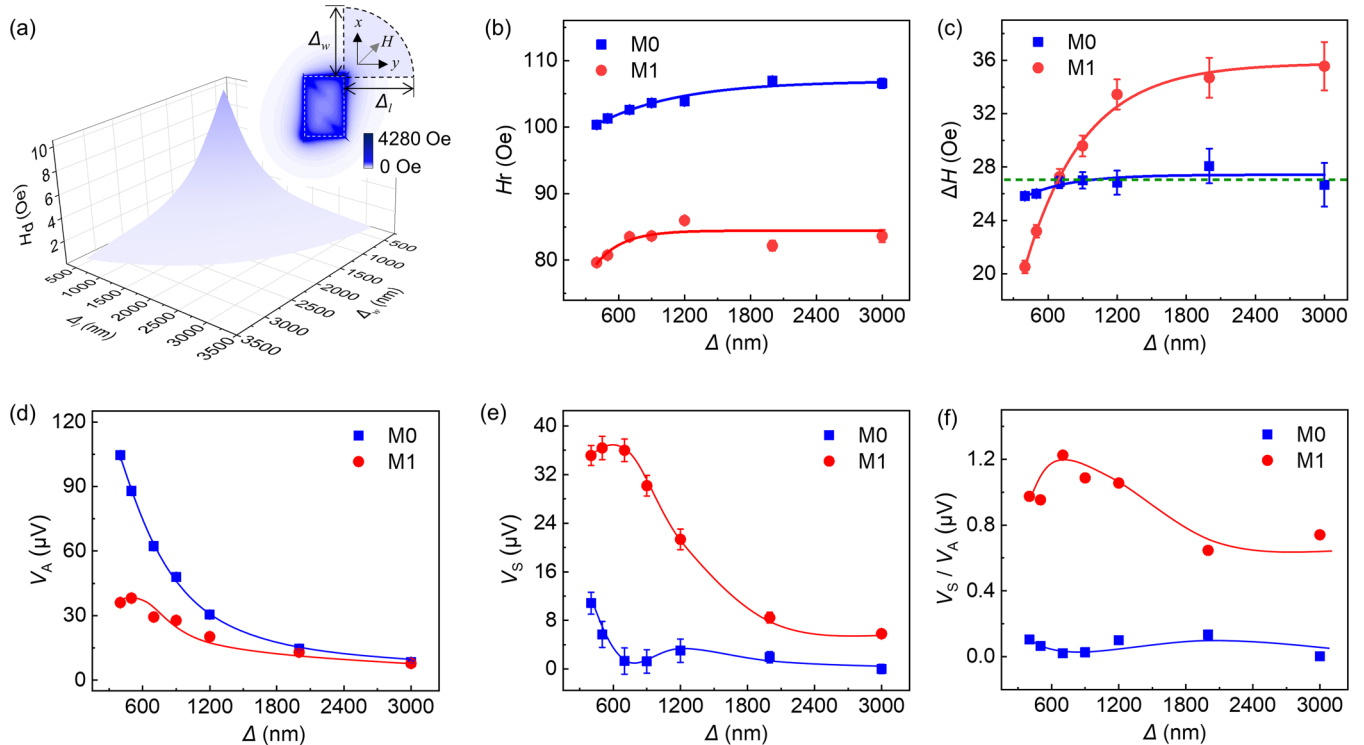


FIG. 4. (a) Spatial distribution of the dipolar field from Py rectangles with  $w = 1 \mu\text{m}$ ,  $l = 1.5 \mu\text{m}$ .  $\Delta_w$  and  $\Delta_l$  denote the distance from the edges of Py rectangle as shown in the inset. (b) Resonance field, (c) linewidth, (d)  $V_A$ , (e)  $V_S$ , (f)  $V_S/V_A$  of M0 and M1 for samples with different  $\Delta$ . The green dashed line in (c) represents the linewidth of Py/Pt with the size of  $20 \mu\text{m} \times 8 \mu\text{m} \times 10 \text{nm}$ . The frequency of the RF current is 3 GHz and the microwave power is 15 dBm. Solid lines serve as visual guides.

induced by SSW may be associated with its distinctive mode structure. Although further investigation is warranted to explore this connection, here we leverage the enhanced spin current generation observed for SSWs to seek experimental evidence of dynamic coupling in the system.

We further turn our attention to the potential coupling among Py arrays. Samples with  $w = 1 \mu\text{m}$ ,  $l = 1.5 \mu\text{m}$ , and  $\Delta = 400 \sim 3000 \text{nm}$  are studied, and the ST-FMR results are shown in Fig. 2(e). Considering the influence of dipolar interactions in our study, we initially simulate the spatial distribution of the dipolar field  $H_d$ . The outcome for a single Py rectangle is illustrated in Fig. 4(a). It is found that  $H_d$  decreases rapidly with increasing distances from the edges of the Py rectangle, thus the effect of  $H_d$  on the neighboring arrays is tiny (see Supplemental Material section S7 [29] for details). Previous studies have shown that dipolar interactions can generally be disregarded when the edge-to-edge spacing between array units exceeds half their diameter [48,49]. For instance, it has been reported that for discs with a diameter of  $1 \mu\text{m}$ , the dipolar interactions between arrays are negligible when the spacing exceeds  $500 \text{nm}$  [49]. In our study, despite employing a rectangular array rather than discs, these findings remain relevant.

The extracted resonance field for samples with varying  $\Delta$  are illustrated in Fig. 4(b). It is observed that below approximately  $700 \text{nm}$ ,  $H_r$  for both M0 and M1 reduce slightly as  $\Delta$  decreases. This reduction is likely caused by magnetic dipolar interactions, contributing to the effective field within the sample. Typically, such magnetic interactions do not involve the magnetic damping term, thus they are not expected to affect

the linewidth magnitude. However, we find it intriguing that the linewidths of both modes narrow with decreasing  $\Delta$  below  $2 \mu\text{m}$ , with M1 showing a particularly significant reduction, as shown in Fig. 4(c). The steady linewidth of M0 in samples with  $\Delta$  above  $2 \mu\text{m}$  is comparable to that of a Py/Pt continuous film [depicted by the green dashed line in Fig. 4(c)], indicating the fabrication homogeneity of our devices. This reduction in linewidth suggests the existence of a coupling effect within the system. Notably, the coupling distance extends up to  $2 \mu\text{m}$ , far exceeding the spin diffusion length of Pt [50,51], possibly resulting from the dynamic coupling of Py elements mediated by electrical current in Pt. Nonetheless, other effects, such as the altered mode profile induced by magnetic dipolar interactions, and the AC component of the spin current and charge current, remain difficult to exclude. We attempt measurements under conditions where the current source is disconnected, thus rendering direct passage of DC charge current through the circuitry challenging. It shows that the linewidth does not exhibit a discernible trend with  $\Delta$  (see Supplemental Material section S7 [29] for details), further corroborating the presence of coupling mediated by the DC charge current within our system.

To differentiate between the contributions of dynamic coupling versus changes in mode profile to linewidth, we further focus on the variation of signal intensity with spacing. It is understood that the detected voltage signal varies with changes in  $\Delta$  due to several influencing factors, specifically: (1) the effective magnetic signal associated with the area of magnetic layers, (2) the microwave power within the device, (3) the magnetic dipolar interactions between ferromagnetic

elements, and (4) the impact of dynamic coupling. Neglecting changes in internal current distribution, the effects of magnetic layer area, microwave power, and magnetic dipolar interactions on both  $V_S$  and  $V_A$  for the same mode are expected to be consistent. This results in both  $V_S$  and  $V_A$  increasing (or decreasing) as the spacing decreases, while the ratio  $V_S/V_A$  remains largely unchanged. Dipolar interactions may influence the mode profile, enhancing the  $V_S$  and  $V_A$  of M0 while reducing those of M1. Importantly, dynamic coupling affects different modes and their respective variations in  $V_S$  and  $V_A$  differently: when magnetic moments undergo coupled precession at a specific frequency, their precession intensity increases and linewidth decreases, leading to an increase in spin currents within the system while charge currents remain relatively stable. Consequently, both  $V_S$  and  $V_S/V_A$  increase in this scenario.

The variations of  $V_A$ ,  $V_S$  and their ratio with respect to  $\Delta$  are accurately captured in Figs. 4(d)–4(f). With decreased  $\Delta$ ,  $V_A$  for both M0 and M1 shows significant enhancement due to reduced device resistance that lowers microwave losses in the circuit (See Supplemental Material section S8 [29]). Within spacing distances of approximately 700 nm, both  $V_S$  and  $V_A$  of M0 tend to increase as  $\Delta$  decreases, while those of M1 exhibit a decreasing trend. This phenomenon may be attributed to changes in the mode profile induced by dipolar interactions. Comparing these outcomes with the resonance field variations depicted in Fig. 4(c), we confirm that dipolar interactions influence the FMR spectra when  $\Delta$  is below 700 nm. However, as the spacing increases beyond 700 nm, we observe a notable decrease followed by stabilization in  $V_S$  and  $V_S/V_A$  for M1. Together with the significant linewidth reduction of M1 within this distance region shown in Fig. 4(c), these observations underscore the dominant impact of dynamic coupling for M1 within this specific distance range. This pronounced coupling effect may be attributed to M1 exhibiting a more substantial spin pumping effect compared to M0.

In conclusion, our study proposes an approach for achieving long-distance coupling between ferromagnets via a charge current in a nonmagnetic heavy metal. The theoretical results elucidates the dissipative nature of this dynamic coupling, characterized by energy-level attraction that facilitates synchronization of frequency, phase, and amplitude information. Experimental investigations on interconnected Py arrays via Pt strips further validate this dynamic coupling. Two confined precession modes, the quasiuniform precession mode M0 and the SSW mode M1, in submicrometer-sized Py rectangles interconnected by Pt strips are detected using ST-FMR. Results indicate that the SSW mode generates a significantly larger spin current compared to the quasiuniform precession mode, as evidenced by the increased symmetry component and the nonlinear power dependence of the output voltage. Notably, a coupling effect is observed among Py arrays, characterized by reduced linewidths, with coupling distances extending up to 2  $\mu\text{m}$ . Within distances of 700 nm, this coupling effect is coinfluenced by dipolar interactions and dynamic coupling mediated by the charge current. Beyond 700 nm, dynamic coupling predominates. The observed effects are detectable due to array superposition and efficient spin pumping of the SSW mode. These findings propose a promising strategy for long-distance interaction and synchronization in magnonic devices.

The authors thank G. E. W. Bauer for fruitful discussions. This work is supported by the National Key Research and Development Program of China (Grant No. 2023YFA1406600), National Natural Science Foundation of China (Grants No. 52071079, No. 12274071, No. 52371206, and No. 12474127), the Jiangxi Province Double Thousand Plan (Grant No. S2019CQKJ2638), Jiangsu Funding Program for Excellent Postdoctoral Talent (Grant No. 2023ZB491) and Gusu Leading Talents Program (Grant No. ZXL2023172).

- 
- [1] S. Kaka, M. R. Pufall, W. H. Rippard, T. J. Silva, S. E. Russek, and J. A. Katine, Mutual phase-locking of microwave spin torque nano-oscillators, *Nature (London)* **437**, 389 (2005).
  - [2] F. B. Mancoff, N. D. Rizzo, B. N. Engel, and S. Tehrani, Phase-locking in double-point-contact spin-transfer devices, *Nature (London)* **437**, 393 (2005).
  - [3] D. MacNeill, J. T. Hou, D. R. Klein, P. Zhang, P. Jarillo-Herrero, and L. Liu, Gigahertz frequency antiferromagnetic resonance and strong magnon-magnon coupling in the layered crystal  $\text{CrCl}_3$ , *Phys. Rev. Lett.* **123**, 047204 (2019).
  - [4] J. Chen, C. Liu, T. Liu, Y. Xiao, K. Xia, G. E. W. Bauer, M. Wu, and H. Yu, Strong interlayer magnon-magnon coupling in magnetic metal-insulator hybrid nanostructures, *Phys. Rev. Lett.* **120**, 217202 (2018).
  - [5] M. R. Pufall, W. H. Rippard, S. E. Russek, S. Kaka, and J. A. Katine, Electrical measurement of spin-wave interactions of proximate spin transfer nanooscillators, *Phys. Rev. Lett.* **97**, 087206 (2006).
  - [6] B. Heinrich, Y. Tserkovnyak, G. Woltersdorf, A. Brataas, R. Urban, and G. E. W. Bauer, Dynamic exchange coupling in magnetic bilayers, *Phys. Rev. Lett.* **90**, 187601 (2003).
  - [7] Y. Tserkovnyak, A. Brataas, and G. E. W. Bauer, Enhanced Gilbert damping in thin ferromagnetic films, *Phys. Rev. Lett.* **88**, 117601 (2002).
  - [8] T. Taniguchi, Phase dynamics of oscillating magnetizations coupled via spin pumping, *Phys. Rev. B* **97**, 184408 (2018).
  - [9] B. Zare Rameshti and G. E. W. Bauer, Indirect coupling of magnons by cavity photons, *Phys. Rev. B* **97**, 014419 (2018).
  - [10] V. L. Grigoryan and K. Xia, Cavity-mediated dissipative spin-spin coupling, *Phys. Rev. B* **100**, 014415 (2019).
  - [11] Y. Li, V. G. Yefremenko, M. Lisovenko, C. Trevillian, T. Polakovic, T. W. Cecil, P. S. Barry, J. Pearson, R. Divan, V. Tyberkevych, C. L. Chang, U. Welp, W.-K. Kwok, and V. Novosad, Coherent coupling of two remote magnonic resonators mediated by superconducting circuits, *Phys. Rev. Lett.* **128**, 047701 (2022).
  - [12] H. Pan, Z. H. An, and C. M. Hu, Magnon-magnon coupling mediated by topological edge states, *Phys. Rev. Res.* **6**, 013020 (2024).
  - [13] K. An, A. N. Litvinenko, R. Kohno, A. A. Fuad, V. V. Naletov, L. Vila, U. Ebels, G. de Loubens, H. Hurdequint, N. Beaulieu, J. Ben Youssef, N. Vukadinovic, G. E. W. Bauer, A. N. Slavin,

- V. S. Tiberkevich, and O. Klein, Coherent long-range transfer of angular momentum between magnon Kittel modes by phonons, *Phys. Rev. B* **101**, 060407(R) (2020).
- [14] W. Yu, Dynamic exchange coupling between magnets mediated by attenuated elastic waves, *Phys. Rev. B* **108**, 134414 (2023).
- [15] T. Taniguchi, Dynamic coupling of ferromagnets via spin Hall magnetoresistance, *Phys. Rev. B* **95**, 104426 (2017).
- [16] M. Weiler, J. M. Shaw, H. T. Nembach, and T. J. Silva, Phase-sensitive detection of spin pumping via the AC inverse spin Hall effect, *Phys. Rev. Lett.* **113**, 157204 (2014).
- [17] D. Wei, M. Obstbaum, M. Ribow, C. H. Back, and G. Woltersdorf, Spin Hall voltages from a.c. and d.c. spin currents, *Nat. Commun.* **5**, 3768 (2014).
- [18] H. Jiao and G. E. Bauer, Spin backflow and AC voltage generation by spin pumping and the inverse spin hall effect, *Phys. Rev. Lett.* **110**, 217602 (2013).
- [19] C. Hahn, G. de Loubens, M. Viret, O. Klein, V. V. Naletov, and J. Ben Youssef, Detection of microwave spin pumping using the inverse spin hall effect, *Phys. Rev. Lett.* **111**, 217204 (2013).
- [20] J. Sinova, S. O. Valenzuela, J. Wunderlich, C. H. Back, and T. Jungwirth, Spin Hall effects, *Rev. Mod. Phys.* **87**, 1213 (2015).
- [21] K. Garello, I. M. Miron, C. O. Avci, F. Freimuth, Y. Mokrousov, S. Blügel, S. Auffret, O. Boulle, G. Gaudin, and P. Gambardella, Symmetry and magnitude of spin-orbit torques in ferromagnetic heterostructures, *Nat. Nanotechnol.* **8**, 587 (2013).
- [22] A. Hamadeh, O. d'Allivy Kelly, C. Hahn, H. Meley, R. Bernard, A. H. Molpeceres, V. V. Naletov, M. Viret, A. Anane, V. Cros, S. O. Demokritov, J. L. Prieto, M. Muñoz, G. de Loubens, and O. Klein, Full control of the spin-wave damping in a magnetic insulator using spin-orbit torque, *Phys. Rev. Lett.* **113**, 197203 (2014).
- [23] L. Zhu, D. C. Ralph, and R. A. Buhrman, Spin-orbit torques in heavy-metal-ferromagnet bilayers with varying strengths of interfacial spin-orbit coupling, *Phys. Rev. Lett.* **122**, 077201 (2019).
- [24] A. Manchon, J. Železný, I. M. Miron, T. Jungwirth, J. Sinova, A. Thiaville, K. Garello, and P. Gambardella, Current-induced spin-orbit torques in ferromagnetic and antiferromagnetic systems, *Rev. Mod. Phys.* **91**, 035004 (2019).
- [25] O. Mosendz, J. E. Pearson, F. Y. Fradin, G. E. W. Bauer, S. D. Bader, and A. Hoffmann, Quantifying spin Hall angles from spin pumping: Experiments and theory, *Phys. Rev. Lett.* **104**, 046601 (2010).
- [26] Y. Tserkovnyak, A. Brataas, G. E. W. Bauer, and B. I. Halperin, Nonlocal magnetization dynamics in ferromagnetic heterostructures, *Rev. Mod. Phys.* **77**, 1375 (2005).
- [27] M. Tokaç, S. A. Bunyaev, G. N. Kakazei, D. S. Schmool, D. Atkinson, and A. T. Hindmarch, Interfacial structure dependent spin mixing conductance in cobalt thin films, *Phys. Rev. Lett.* **115**, 056601 (2015).
- [28] L. Liu, T. Moriyama, D. C. Ralph, and R. A. Buhrman, Spin-torque ferromagnetic resonance induced by the spin Hall effect, *Phys. Rev. Lett.* **106**, 036601 (2011).
- [29] See Supplemental Material at <http://link.aps.org/supplemental/10.1103/PhysRevB.110.224427> for the quantitative discussion of the dynamic coupling; measurement circuit details; fabrication and structure of the device; micromagnetic simulation of precession modes in Py rectangles; fitting details of the ST-FMR spectrum; discussions on spin current pumped from different precession modes; influences of other interactions; and variation of device resistance with spacing, which also contains Refs. [26–28,37,38].
- [30] M. Harder, Y. Yang, B. M. Yao, C. H. Yu, J. W. Rao, Y. S. Gui, R. L. Stamps, and C. M. Hu, Level attraction due to dissipative magnon-photon coupling, *Phys. Rev. Lett.* **121**, 137203 (2018).
- [31] V. L. Grigoryan, K. Shen, and K. Xia, Synchronized spin-photon coupling in a microwave cavity, *Phys. Rev. B* **98**, 024406 (2018).
- [32] W. Yu, J. Wang, H. Y. Yuan, and J. Xiao, Prediction of attractive level crossing via a dissipative mode, *Phys. Rev. Lett.* **123**, 227201 (2019).
- [33] P. Carrara, M. Brioschi, R. Silvani, A. O. Adeyeye, G. Panaccione, G. Gubbiotti, G. Rossi, and R. Cucini, Coherent and dissipative coupling in a magnetomechanical system, *Phys. Rev. Lett.* **132**, 216701 (2024).
- [34] J. Zou, S. Bosco, E. Thingstad, J. Klinovaja, and D. Loss, Dissipative spin-wave diode and nonreciprocal magnonic amplifier, *Phys. Rev. Lett.* **132**, 036701 (2024).
- [35] N. Kuhlmann, A. Vogel, and G. Meier, Magnetization dynamics and cone angle precession in permalloy rectangles, *Phys. Rev. B* **85**, 014410 (2012).
- [36] M. B. Jungfleisch, J. Ding, W. Zhang, W. Jiang, J. E. Pearson, V. Novosad, and A. Hoffmann, Insulating nanomagnets driven by spin torque, *Nano Lett.*, **17**, 8 (2017).
- [37] M. J. Donahue and D. G. Porter, *OOMMF User's Guide Version 1.0*. (National Institute of Standards and Technology, Gaithersburg, MD, 1999), <http://math.nist.gov/oommf/>.
- [38] M. Frankowski, J. Chęciński, and M. Czapkiewicz, Spatial spectrum analyzer (SSA): A tool for calculations of spatial distribution of fast Fourier transform spectrum from object oriented micromagnetic framework output data, *Comp. Phys. Commun.* **189**, 207 (2015).
- [39] Z. Zeng, K. H. Cheung, H. W. Jiang, I. N. Krivorotov, J. A. Katine, V. Tiberkevich, and A. Slavin, Evolution of spin-wave modes in magnetic tunnel junction nanopillars, *Phys. Rev. B* **82**, 100410(R) (2010).
- [40] J. Stigloher, M. Decker, H. S. Körner, K. Tanabe, T. Moriyama, T. Taniguchi, H. Hata, M. Madami, G. Gubbiotti, K. Kobayashi, T. Ono, and C. H. Back, Snell's Law for spin waves, *Phys. Rev. Lett.* **117**, 037204 (2016).
- [41] B. A. Kalinikos and A. N. Slavin, Theory of dipole-exchange spin wave spectrum for ferromagnetic films with mixed exchange boundary conditions, *J. Phys. C* **19**, 7013 (1986).
- [42] K. Kondou, H. Sukegawa, S. Kasai, S. Mitani, Y. Niimi, and Y. Otani, Influence of inverse spin Hall effect in spin-torque ferromagnetic resonance measurements, *Appl. Phys. Express* **9**, 023002 (2016).
- [43] Y. Zhang, Q. Liu, B. F. Miao, H. F. Ding, and X. R. Wang, Anatomy of electrical signals and DC-voltage line shape in spin-torque ferromagnetic resonance, *Phys. Rev. B* **99**, 064424 (2019).
- [44] H. Nakayama, K. Ando, K. Harii, T. Yoshino, R. Takahashi, Y. Kajiwara, K. Uchida, Y. Fujikawa, and E. Saitoh, Geometry dependence on inverse spin Hall effect induced by spin pumping in Ni<sub>81</sub>Fe<sub>19</sub>/Pt films, *Phys. Rev. B* **85**, 144408 (2012).
- [45] Y. S. Chen, J. G. Lin, S. Y. Huang, and C. L. Chien, Incoherent spin pumping from YIG single crystals, *Phys. Rev. B* **99**, 220402(R) (2019).

- [46] C. W. Sandweg, Y. Kajiwara, K. Ando, E. Saitoh, and B. Hillebrands, Enhancement of the spin pumping efficiency by spin wave mode selection, *Appl. Phys. Lett.* **97**, 252504 (2010).
- [47] Y. Kajiwara, K. Harii, S. Takahashi, J. Ohe, K. Uchida, M. Mizuguchi, H. Umezawa, H. Kawai, K. Ando, K. Takanashi, S. Maekawa, and E. Saitoh, Transmission of electrical signals by spin-wave interconversion in a magnetic insulator, *Nature (London)* **464**, 262 (2010).
- [48] K. Y. Guslienko, Magnetostatic interdot coupling in two-dimensional magnetic dot arrays, *Appl. Phys. Lett.* **75**, 394 (1999).
- [49] A. Vogel, A. Drews, T. Kamionka, M. Bolte, and G. Meier, Influence of dipolar interaction on vortex dynamics in arrays of ferromagnetic disks, *Phys. Rev. Lett.* **105**, 037201 (2010).
- [50] M.-H. Nguyen, D. C. Ralph, and R. A. Buhrman, Spin torque study of the spin Hall conductivity and spin diffusion length in platinum thin films with varying resistivity, *Phys. Rev. Lett.* **116**, 126601 (2016).
- [51] C. Gonzalez-Fuentes, R. Henriquez, C. García, R. K. Dumas, B. Bozzo, and A. Pomar, Spin diffusion length associated with out-of-plane conductivity of Pt in spin pumping experiments, *Phys. Rev. B* **103**, 224403 (2021).